

# Abrupt Reduction in Shipping Emission as an Inadvertent Geoengineering Termination Shock Produces Substantial Radiative Warming

Tianle Yuan<sup>1,2,\*</sup>, Hua Song<sup>2,3</sup>, Lazaros Oreopoulos<sup>2</sup>, Robert Wood<sup>4</sup>, Huisheng Bian<sup>1,2</sup>, Katherine Breen<sup>2,5</sup>, Mian Chin<sup>2</sup>, Hongbin Yu<sup>2</sup>, Donifan Barahona<sup>2</sup>, Kerry Meyer<sup>2</sup>, Steven Platnick<sup>2</sup>,

<sup>1</sup>GESTAR-II, University of Maryland, Baltimore County, Maryland, USA

<sup>2</sup>Sciences and Exploration Directorate, Goddard Space Flight Center, Greenbelt, Maryland, USA

<sup>3</sup>SSAI, Inc., Lanham, Maryland, USA

<sup>4</sup>Department of Atmospheric Sciences, University of Washington, Seattle, Washington, USA

<sup>5</sup>GESTAR-II, Morgan State University, Baltimore, Maryland, USA

\*Corresponding author: tianle.yuan@nasa.gov

## Abstract

Human activities affect the Earth's climate through modifying the composition of the atmosphere, which then creates radiative forcing that drives climate change. The warming effect of anthropogenic greenhouse gases has been partially balanced by the cooling effect of anthropogenic aerosols. In 2020, fuel regulations abruptly reduced the emission of sulfur dioxide from international shipping by about 80% and created an inadvertent geoengineering termination shock with global impact. Here we estimate the regulation leads to a radiative forcing of  $+0.2 \pm 0.11 \text{ Wm}^{-2}$  averaged over the global ocean. The amount of radiative forcing could lead to a doubling (or more) of the warming rate in the 2020s compared with the rate since 1980 with strong spatiotemporal heterogeneity. The warming effect is consistent with the recent observed strong warming in 2023 and expected to make the 2020s anomalously warm. The forcing represents 80% to the measured increase in planetary heat uptake since 2020. The radiative forcing also has strong hemispheric contrast, which has important implications for precipitation pattern changes. Our result suggests marine cloud brightening may be a viable geoengineering method in temporarily cooling the climate that has its unique challenges due to inherent spatiotemporal heterogeneity.

1 **Text**

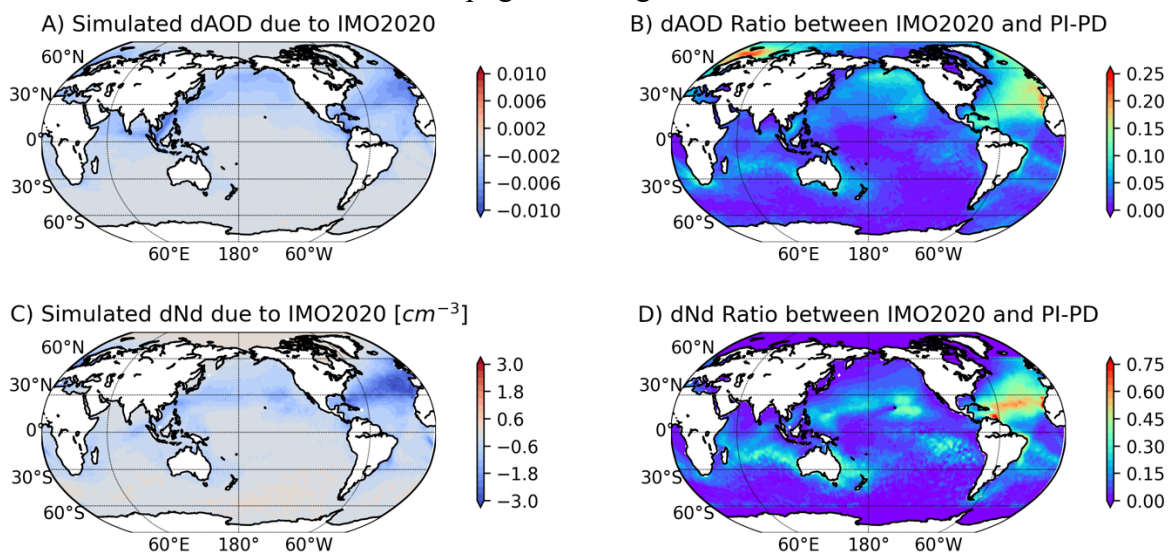
2 The Earth's atmosphere has warmed because of human activities increasing the concentration of  
3 greenhouse gases that trap thermal radiative energy in the climate system, creating a positive  
4 climate forcing. Human activities have also increased the concentration of aerosol particles that  
5 can affect the amount of reflected solar radiation back to space either directly or indirectly by  
6 interacting with clouds, which has an overall cooling effect on the climate <sup>1</sup>. The magnitude of  
7 the aerosol cooling effect has significant implications for estimating how sensitive our climate is  
8 to greenhouse gas forcing and the amount of expected future warming for a given increase of  
9 greenhouse gas concentrations <sup>2</sup>. The effectiveness of anthropogenic aerosols in cooling the  
10 climate also has direct implications for solar radiation modification geoengineering schemes <sup>3,4</sup>.  
11 Such methods aim to produce temporary cooling of the climate through enhanced reflection  
12 of solar radiation to space. They are not solutions to greenhouse gas induced global warming and  
13 have uncertain and complex additional consequences besides the intended short-term cooling  
14 effect <sup>4-7</sup>.

15  
16 Marine cloud brightening (MCB) is a type of solar radiation modification scheme where marine  
17 low clouds are seeded with aerosols to become brighter <sup>8,9</sup>. Examples of small scale,  
18 opportunistic MCB experiments were discovered in early satellite observations of ship-tracks,  
19 linear features of brighter oceanic clouds because of ship-emitted aerosols <sup>10,11</sup>. The addition of  
20 aerosols from ship emissions results in more cloud droplets, leading to more reflective clouds for  
21 a given amount of total In-cloud liquid water, or liquid water path (LWP) <sup>12</sup>. More recent studies  
22 show that aerosols can also change LWP and total cloud fraction (CF), which also greatly affect  
23 the amount of solar radiation reflected by clouds <sup>2,13-16</sup>.

24  
25 Aerosols sourced from global shipping industry affect clouds and we can view the shipping  
26 emission as a long-running inadvertent MCB experiment. On January 1, 2020, new International  
27 Maritime Organization (IMO) regulations on the sulfur content of international shipping fuel  
28 took effect. The IMO 2020 regulation (IMO2020) reduced the maximum sulfur content from  
29 3.5% to 0.5% <sup>17</sup>. While IMO2020 is intended to benefit public health by decreasing aerosol  
30 loading, this decrease in aerosols can temporarily accelerate global warming by dimming clouds  
31 across the global oceans. IMO2020 took effect in a short period of time and likely has global  
32 impact. IMO2020 effectively represents a termination shock for the inadvertent geoengineering  
33 experiment through a reverse MCB, i.e., marine cloud dimming through reducing cloud droplet  
34 number concentration ( $N_d$ ) (Figure 1). Observations of ship-tracks suggest that IMO2020 has  
35 reduced the occurrence and modified the properties of ship-tracks across global oceans,  
36 demonstrating that a regulation intended to reduce pollution had collateral effects on cloud  
37 microphysics <sup>18</sup>. Analyses of remote sensing data have shown evidence of cloud dimming in the  
38 South Atlantic shipping lane <sup>19</sup>. Outside the South Atlantic, the effect of IMO2020 does not have  
39 a distinct spatial structure <sup>18,19</sup>, which makes direct observation of the impact more challenging.

40  
41 Here we combine satellite observations and a chemical transport model to quantify the radiative  
42 forcing of the inadvertent geoengineering event induced by IMO2020 and estimate its climate  
43 impacts. We simulate the impact of IMO2020 on maritime aerosol concentrations with the  
44 NASA GEOS-GOCART model. Figure 1 shows the modeled reduction in aerosol optical depth  
45 due to decreased SO<sub>2</sub> emission from the international shipping industry. The AOD reduction  
46 reaches peak values of around 0.01 in the South China Sea and Eastern North Atlantic off the

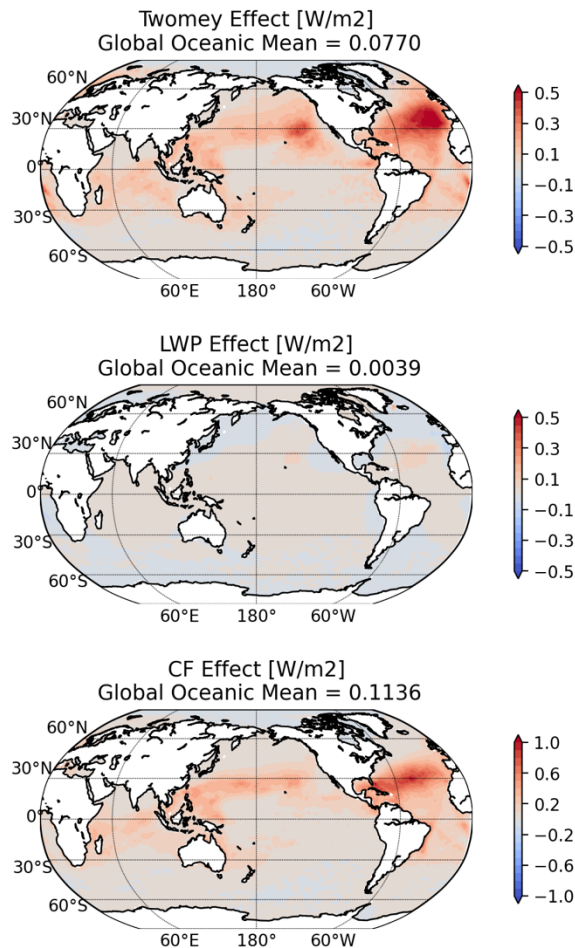
1 coasts of Western Europe. In the South Atlantic the regulations create AOD reductions that  
 2 follow the shape of shipping routes. We then calculate the ratio between the AOD change due to  
 3 IMO2020 and that between pre-industrial and present day. Over most of the ocean, the ratio is  
 4 smaller than 10% because of sparse shipping outside the major shipping routes. Over the North  
 5 Pacific and North Atlantic, on the other hand, it can exceed 10% and reaches 25% in the  
 6 Norwegian Sea and off the western European and northwestern African coasts. In these regions,  
 7 the total anthropogenic aerosol concentration is relatively low because of declining emissions of  
 8 aerosols and their precursors since the 1980s, making ship-emitted aerosols an important  
 9 component of the anthropogenic maritime aerosols. The IMO2020 is therefore effective in  
 10 reducing total aerosol loading for these regions. The impact of IMO2020 on the cloud droplet  
 11 number concentration ( $N_d$ ) of low-level maritime clouds as shown in Figure 1C (see Methods).  
 12 Globally, IMO2020 leads to a modest reduction of  $0.5 \text{ cm}^{-3}$  in mean modeled  $N_d$ . Regionally,  
 13 however, the reduction is more pronounced. The strongest reduction occurs in the North Atlantic,  
 14 the Caribbeans and the South China Sea, reaching  $3 \text{ cm}^{-3}$ . These are regions with the busiest  
 15 shipping lanes and thus strongest reduction of ship emissions. The reduction in the South  
 16 Atlantic shows the most well-defined shipping lane shapes likely due to the unique circulation  
 17 pattern in this region<sup>18,20</sup>. Figure 1d shows the ratio between IMO2020 induced  $N_d$  decrease and  
 18 estimated  $N_d$  difference between preindustrial and present day. The ratio is small over the major  
 19 outflow areas downwind of major continental sources, but becomes substantially larger in more  
 20 remote oceans, reaching 30%. In the tropical North Atlantic, IMO2020 induced change in  $N_d$  can  
 21 be more than 50% of the total anthropogenic change.



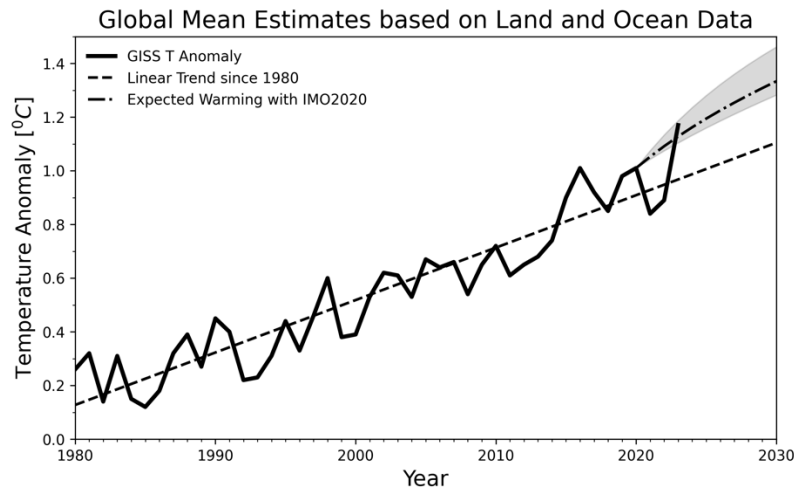
22  
 23 **Figure 1 Simulated impact of IMO2020 on AOD and  $N_d$ . a) simulated annual mean aerosol**  
 24 **optical depth change induced by IMO2020 using NASA GOES-GOCART. b) the ratio of**  
 25 **aerosol optical depth changes between that induced by IMO2020 and that between 1750**  
 26 **and 2005<sup>2</sup>. c) map of simulated annual mean  $N_d$  change due to IMO2020. d) same as b, but**  
 27 **for  $N_d$  change.**

28  
 29 We combine  $N_d$  changes due to IMO2020 with satellite observations to estimate the forcing  
 30 introduced by the inadvertent geoengineering event<sup>21</sup>. We consider both the Twomey effect and  
 31 the effects of cloud liquid water path (LWP) and cloud fraction adjustments to  $N_d$  (see Methods  
 32 section). The LWP and cloud fraction adjustments follow the functional forms derived from a

1 large sample of ship-tracks<sup>21</sup> that depend on the background cloud  $N_d$ , sea surface temperature  
2 (SST), estimated inversion strength, and background low cloud fraction (see Methods). Figure 2  
3 shows the pattern of annual mean of forcing resulting from  $N_d$  decrease due to IMO2020  
4 averaged over different LWP and cloud fraction adjustment functional forms. The total forcing is  
5  $+0.2 \pm 0.11 \text{Wm}^{-2}$  averaged over the global ocean with the Twomey effect contributing 40%, the  
6 LWP adjustment being near neutral, and the cloud fraction adjustment contributing 60%. The  
7 positive radiative forcing has strong regional variations. The North Atlantic experiences the  
8 strongest radiative forcing peaking around  $1.4 \text{Wm}^{-2}$  and whose basin-wide mean is around  
9  $0.56 \text{Wm}^{-2}$ . Weaker but still notable radiative forcing is seen in the North Pacific and the South  
10 Atlantic. This ordering is consistent with the amount of ship traffic and low cloud fraction in  
11 these regions. Our estimate of radiative forcing from IMO2020 is well within the range of  
12 estimates of the total forcing from shipping emissions in the literature<sup>22–25</sup>. We also compare our  
13 estimate with that from a recent observational study in the core shipping lane in the South  
14 Atlantic that used a different approach<sup>19</sup>. The two completely independent approaches yield very  
15 similar radiative forcing in the core shipping lane (supporting online material, SOM), which  
16 serves as a cross-validation. Similar global forcing, i.e., on the order of  $0.1 \text{Wm}^{-2}$ , is reported by  
17 multiple modeling groups<sup>26</sup>.



18  
19 **Figure 2: Calculated IMO2020 forcing maps from different components. The spatial**  
20 **patterns of three components of forcing from cloud adjustments: a) the Twomey effect, b)**  
21 **LWP adjustment, and c) cloud fraction adjustment.**

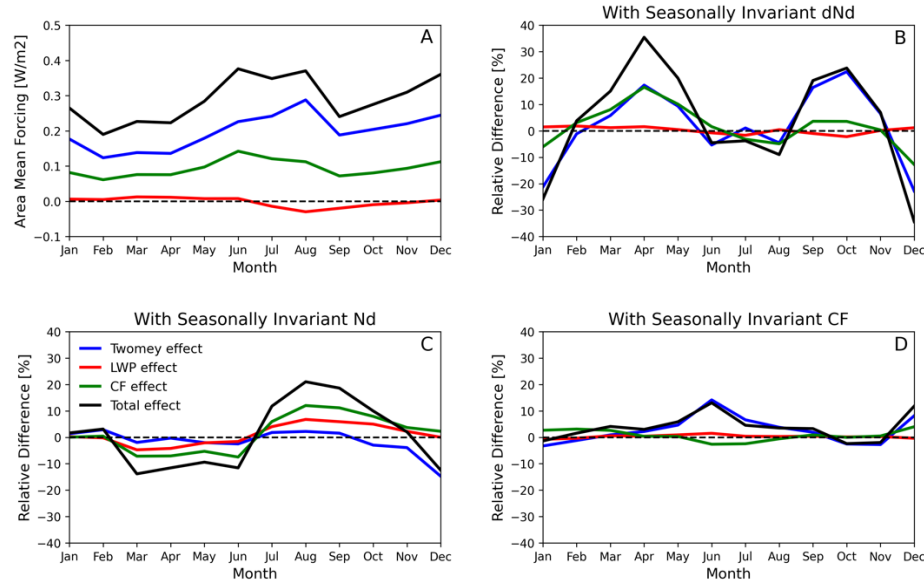


2

3 **Figure 3: Time series of global temperature anomaly since the 1980 (Lensen et al., 2019).**  
 4 **The trend line is dashed. The expected warming trajectory from the combination of the**  
 5 **linear trend and the calculated warming effect from IMO 2020 shock based on the energy**  
 6 **balance model. The upper and lower bounds of the expected warming are shown in shades.**  
 7 **The baseline period for temperature anomaly is between 1951 and 1980.**

8

9 Using an energy balance model<sup>27</sup>, we calculate the expected amount of transient temperature  
 10 increase due to warming resulting from IMO2020. For simplicity, we ignore the heat uptake by  
 11 the deep ocean during the short-term, i.e.  $O(10)$  years.  $0.2\text{Wm}^{-2}$  translates to around  $0.16\text{K}$  of  
 12 warming with a timescale of 7 years. It is equivalent to  $0.24\text{K/decade}$ , which is more than double  
 13 the average warming rate since 1880 and 20% higher than the mean warming rate since 1980,  
 14 linear trend of  $0.19\text{K/decade}$ . We also calculated the lower and upper bounds of the forcing and  
 15 corresponding expected warming (Figure 3). The IMO2020 is expected to provide a substantial  
 16 boost to the warming rate of global mean temperature in the 2020s. The rate of warming is  
 17 expected to ramp up quickly from 2020 and asymptotes to the longer-term trend line at the end of  
 18 2020<sup>27</sup>. The 2023 record warmth is within the ranges of our expected trajectory. The magnitude  
 19 of IMO2020 induced warming means that the observed strong warming in 2023 will be a new  
 20 norm in the 2020s. The mean temperature anomaly of the 2020s will be  $0.3\text{K}$  higher than that of  
 21 the 2010s. Regionally, the warming effect from IMO2020 on SST is harder to estimate since  
 22 basin-wide SST changes can be affected by variations in factors like other aerosol concentration,  
 23 ocean circulation, and air-sea interactions. However, the strong geographical variations in the  
 24 forcing suggest the impact of IMO2020 on SST may have significant variation among ocean  
 25 basins. For example, the North Atlantic SST may be disproportionately warmed more by the  
 26 IMO2020 given the radiative forcing is more than three times the global average, which is likely  
 27 a contributing factor to the pronounced warming of the North Atlantic SST in recent years<sup>28</sup>. A  
 28 more robust quantitative estimate of the contribution of IMO2020 to regional SST warming  
 29 requires coupled global climate models that have good representation of aerosol indirect effects.

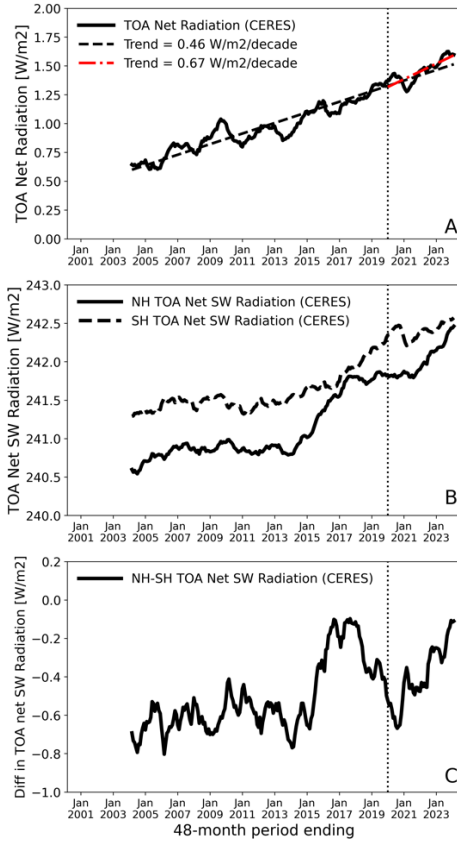


1  
2 **Figure 4: Sensitivity of forcing components to different cloud variables. a) The areal mean**  
3 **of forcing from IMO2020 in the North Atlantic ( $0^{\circ}$ - $80^{\circ}$ W,  $0^{\circ}$  ~  $60^{\circ}$ N) and its break down in**  
4 **three components. b-d) sensitivity tests to gauge the impacts of seasonal variations in  $\Delta N_d$ ,**  
5 **background  $N_d$ , and cloud fraction, respectively. In each test, we use an annual mean map**  
6 **instead of seasonally changing fields to calculate the radiative forcing and plot their**  
7 **difference from the baseline. Details in Methods section.**

8  
9 The IMO2020-induced radiative forcing exhibits considerable seasonal variations. This is  
10 evident in the North Atlantic where the IMO2020 produced the strongest forcing. Figure 4 shows  
11 the monthly mean time series of forcing and its three components. We use a simple functional  
12 form for cloud adjustments that only depends on background  $N_d$  to illustrate the point. The total  
13 forcing varies between  $0.19\text{Wm}^{-2}$  and  $0.38\text{Wm}^{-2}$ , a 100% relative change. The seasonal variation  
14 of incoming solar radiation is the dominant driver for this (SOM). But seasonal variations of  
15 background CF,  $N_d$ , and  $\Delta N_d$  due to IMO2020 also contribute as they affect the magnitude of the  
16 Twomey effect and macrophysical (LWP and CF) cloud adjustments. We estimate the  
17 contribution from each variable after removing the seasonal change in solar insolation, and report  
18 the results in Figure 4b-d (see Methods).  $\Delta N_d$  induced by IMO2020 is the strongest contributor.  
19 Its variations can affect the forcing by more than 30% in some months such as Jan, Apr, and Dec.  
20 Its impact on LWP and CF adjustments contributes equally to the total radiative forcing. The  
21 seasonal variation of background  $N_d$  is also an important factor (Figure 4c). Background CF also  
22 meaningfully contributes to the seasonal variations through mostly affecting the Twomey effect  
23 (Figure 4d).

24  
25 We compare the radiative forcing due to IMO2020 and its effect on radiative energy balance with  
26 observed changes in relevant quantities. The comparison does not prove causality but provides a  
27 context to assess the impact of IMO2020. The low cloud dimming forcing of  $0.2\text{Wm}^{-2}$  from the  
28 IMO2020 represents a strong temporary shock to the net planetary heat uptake (Figure 5a) that  
29 has been increasing at a rate of  $\sim 0.05\text{Wm}^{-2}/\text{yr}$ <sup>29</sup> in measurements. The net planetary heat uptake  
30 has increased by  $0.25\text{Wm}^{-2}$  since 2020, making the  $0.2\text{Wm}^{-2}$  due to IMO2020 nearly 80% of the  
31 total increase. The long-term trend of CERES TOA net radiation is  $0.46\text{Wm}^{-2}/\text{decade}$  while it

1 changes to  $0.67\text{Wm}^{-2}/\text{decade}$  since IMO2020 took effect. The difference is  $0.21\text{Wm}^{-2}$  that is  
2 consistent with our estimated forcing. However, the record since 2020 is too short to ascertain  
3 the impact of IMO2020 on the long-term trend of the energy balance given its large interannual  
4 variations. The IMO2020 effect also has an asymmetric impact on aerosol loading in the northern  
5 and southern hemispheres because of higher baseline ship emissions in the northern hemisphere.  
6 This creates interhemispheric contrast in the resulting radiative forcing, which has important  
7 implications for deliberate geoengineering schemes because interhemispheric forcing contrast  
8 can create significant perturbations in precipitation patterns<sup>6</sup>. We calculate the interhemispheric  
9 contrast in IMO2020 induced warming effect to be around  $0.22\text{Wm}^{-2}$ , with the northern  
10 hemisphere at  $0.32\text{Wm}^{-2}$  and the southern hemisphere at  $0.1\text{Wm}^{-2}$ . The  $0.22\text{Wm}^{-2}$  contrast is  
11 substantial when compared with recent measured changes in the interhemispheric contrast in  
12 absorbed solar radiation. Figures 5b&c shows measured time series of top-of-atmosphere (TOA)  
13 absorbed solar radiation of both hemispheres and their contrast, respectively. Since IMO2020  
14 took effect, the northern hemisphere (NH) absorbed solar radiation has increased by  $0.5\text{Wm}^{-2}$   
15 from a plateau between 2017 and 2020 while the southern hemisphere (SH) increased at a much  
16 slower rate. The low cloud dimming effect of IMO2020 represents around 60% of increase in  
17 NH absorbed solar radiation. The interhemispheric contrast in absorbed solar radiation has  
18 increased by  $\sim 0.2\text{Wm}^{-2}$  based on measurements, one of the highest rates of increase during the  
19 whole record, which is almost the same as that induced by low cloud dimming effect of  
20 IMO2020. Another rapid increase period is associated with a phase shift in Pacific Decadal  
21 Oscillation (PDO) starting 2014/2015 followed by a strong El-Nino event<sup>29</sup>. The PDO entered a  
22 negative phase in 2020, which would favor a further decrease in the contrast rather than the  
23 observed increase. It is worth noting that in addition to modes of ocean variability such as PDO  
24 and El-Nino Southern Oscillation may contribute to variations in these quantities<sup>6</sup>.



1  
2 **Figure 5: Observed time series of energy balance variables. A) the planetary heat uptake;**  
3 **B) trailing 48-month mean of absorbed solar radiation for both hemispheres. The 48-month**  
4 **mean is applied to remove high-frequency noise. C) Time series of Interhemispheric**  
5 **contrast in absorbed solar radiation. The vertical dotted line marks the Jan 2020. Details in**  
6 **Methods section.**

7  
8  
9 The combination of modeled  $\Delta N_d$  and observed relationship for LWP and cloud fraction  
10 adjustments show that IMO2020 as a termination shock for the inadvertent geoengineering  
11 experiment of shipping emissions has had a non-trivial warming effect on the climate. The  
12 National Academy of Sciences, Engineering, and Medicines<sup>4</sup> recommended the impact of any  
13 outdoor solar radiation management experiment on global mean temperature to be within  $1 \times 10^{-7}$   
14 K. The forcing magnitude of this inadvertent shock has exceeded this limit by a large margin.  
15 However, it does suggest that MCB is a viable solar radiation modification scheme in  
16 temporarily slowing the rate of climate warming. Our analysis also points to strong  
17 spatiotemporal heterogeneities in the forcing produced by the event. Such heterogeneities need to  
18 be considered in any MCB scheme to minimize their potential undesired impacts on regional  
19 climate in addition to the desired slowing of climate warming rate. Important part of the  
20 heterogeneity exists because of background low cloud distribution and its spatiotemporal  
21 variability creating an interhemispheric contrast of radiative forcing having similar magnitude as  
22 the global mean radiative forcing. Understanding this contrast is important because to achieve  
23 the goal of substantially slowing down the warming rate or limit the maximum warming to be  
24 within  $1.5^{30}$ , much larger forcing than that of IMO2020, but of the opposite sign, would be

1 needed. As a result, the interhemispheric contrast needs to be minimized to avoid substantial  
2 perturbations to regional monsoons and other precipitation patterns. It should be noted that the  
3 forcing due to IMO2020 will take time for it to be directly detectable at the global scale in the  
4 observation records, but regionally, e.g., in the North Atlantic, its impact may be detectable  
5 sooner. Regional radiative forcing is already detectable in the Southeast Atlantic shipping lane<sup>19</sup>.  
6 Finally, an important open question for policy makers to consider is the trade-off between the  
7 benefits of better air quality and the potential cost of additional warming as different parts of the  
8 world have reduced and are going to reduce aerosol pollution<sup>31,32</sup>. The trade-off consideration is  
9 also relevant for deliberate geoengineering schemes to select the right properties of emitted  
10 aerosols.

11  
12 There are several sources of uncertainties in our estimate of the radiative forcing via cloud  
13 dimming induced by IMO2020. A key source is the magnitude of  $N_d$  change. Here the  $N_d$  change  
14 is modeled with a chemical transport model and not constrained with actual observations. The  
15 annual mean change in  $N_d$  ( $0.5\text{cm}^{-3}$ ) is small compared to the background  $N_d$  ( $28\text{cm}^{-3}$ ) and its  
16 variability. Counterfactual analyses of satellite-based  $N_d$  changes due to ship emissions in the  
17 South Atlantic may provide useful regional constraint on  $\Delta N_d$  once there are additional years of  
18 observations<sup>19</sup>. Although adjustments of LWP and cloud fraction are robust given the large  
19 number of samples, they have their own limitations as detailed in previous studies<sup>14,33–36</sup>. One  
20 way to gauge the possible range of uncertainty for our forcing estimate is to compare ours with  
21 that from Diamond (2023)<sup>19</sup> in the South Atlantic (SOM). In the core shipping lane, the forcing is  
22 estimated to peak around  $0.5\text{Wm}^{-2}$ , the Twomey effect being the dominant factor in this region  
23 (see Figure 2), in our analysis in excellent agreement with theirs<sup>19</sup>. The inadvertent nature of  
24 IMO2020 means that the ratio between radiative forcing and changes in aerosol mass is not  
25 optimized. Here we report  $0.2\text{Wm}^{-2}$  for around 3.7 Tg of S reduction, which is much less  
26 efficient than a more optimized scheme due to factors such as emitted aerosol size distribution  
27 and the spatial distribution of emission changes<sup>9</sup>. Finally, our analysis does not consider  
28 feedback processes. The additional warming of the ocean can induce positive feedbacks from  
29 low clouds<sup>37,38</sup>, which can only be addressed in a coupled climate model.

30  
31 In summary, IMO2020 represents a termination shock for the inadvertent geoengineering by  
32 global ship emissions through a reverse MCB and produces a positive forcing of  $+0.2 \pm$   
33  $0.11\text{Wm}^{-2}$ . It is expected to provide strong additional warming rate this decade, more than  
34 doubling the long-term mean warming rate. The forcing has pronounced spatiotemporal  
35 heterogeneity. The IMO2020 effect also contributes to a strong temporary increase to the  
36 planetary heat uptake through cloud dimming, and it is around 80% of the measured increase in  
37 interhemispheric contrast of absorbed solar radiation since 2020. Our results offer useful  
38 guidance for MCB and aerosol-cloud interaction research.

## 39 40 **Methods**

### 41 42 *a) GEOS-GOCART simulation of IMO impact on aerosol fields*

43 All simulation experiments were run with the Goddard Chemistry Aerosol Radiation and  
44 Transport (GOCART) aerosol module<sup>39,40</sup> in NASA Goddard Earth Observing System (GEOS)  
45 Earth System Model (ESM). The GEOS model has a one-moment cloud microphysics module  
46 and a rapid radiation transfer model for general circulation models (RRTMG). Sea surface

1 temperature (SST) for the atmospheric dynamic circulation is provided by the GEOS  
 2 Atmospheric Data Assimilation System (ADAS) that incorporates satellite and in situ SST  
 3 observations. The model is run in the replay mode using meteorological fields from the Modern-  
 4 Era Retrospective Analysis for Research and Applications version 2 (MERRA-2) reanalysis<sup>41</sup>.  
 5 "Replay" mode sets the model dynamic state (winds, pressure, and temperature) every 6 hours to  
 6 the balanced states provided by the Meteorological Reanalysis Field of the Modern Research and  
 7 Applications Reanalysis Version 2 (MERRA-2). We run GEOS at a global horizontal resolution  
 8 of approximately 50 km on a cubic sphere grid and 72 vertical layers from the surface to 0.01  
 9 hPa. The time step for dynamic calculation is 450 seconds. The temporal resolution of the  
 10 radiation is 1 hour. All experiments run from 201910 to 202012, with the first three months as  
 11 the spin up period. We use monthly results in our estimation of forcing.

12

13 **Table S1: A summary of SO<sub>2</sub> emissions under different scenarios**

Experiment <sup>1</sup>	Emi-an <sup>2</sup>	Emi-shp	Emi-vol	Emi-bio	Emi-bb
shpallBAU	41.3 TgS	5.3 TgS	11.4 (TgS)	15.3TgS	1.9 (TgS)
Shp1p7BAU	36.8	0.8			
Shp0BAU	36	0			
shpallCovid	36.4	4.4			
Shp1p7Covid	32.6	0.7			
Shp0Covid	32	0			

14 <sup>1</sup>Experimental data for 2020

15 <sup>2</sup>Emi-an: include nine sectors of energy, industry, road transportation, residential, waste,  
 16 agriculture, solvent, shipping, and air traffic.

17

18 We have two set of experiments: business as usual (BAU) and Covid impact (Covid) emissions.  
 19 The BAU used anthropogenic emissions of aerosols and precursor gases from the Community  
 20 Emission Data System (CEDs)<sup>42</sup> but repeat the 2019 emissions for 2020. The dataset includes  
 21 nine emission sectors (energy, industry, road transportation, residential, waste, agriculture,  
 22 solvent, shipping, and air traffic). Biomass burning emissions were taken from the GSFC-  
 23 developed Quick Fire Emission Dataset (QFED)<sup>43</sup>. Volcanic emissions come from the dataset  
 24 that is based on the satellite volcanic SO<sub>2</sub> observations from the OMI instrument on board the  
 25 Aura satellite. Biogenic emissions were calculated with the Model of Emissions of Gases and  
 26 Aerosols from Nature (MEGAN) that is embedded in GEOS model. The wind-driven emissions,  
 27 such as dust and sea salt, were calculated on-line. Time varying greenhouse gases, such as CO<sub>2</sub>,  
 28 CH<sub>4</sub>, N<sub>2</sub>O and ozone-depleting substances, were provided by CMIP5 project.

29

30 The second set of experiments (Covid) adjusted BAU anthropogenic emission to reflect the  
 31 impact of Covid. Using mobility data from Google and Apple<sup>44</sup>, daily scale factors in 2020 were  
 32 derived on sector bases for ten species including important aerosols and their precursors.  
 33 Because of the rapidly changing emissions due to various timing and strength of lockdown  
 34 measures, daily scale factors were provided not only to scale down emission amounts but also to  
 35 move emissions from monthly to daily. The Covid adjusted daily anthropogenic emissions were  
 36 generated by applying these scale factors to CEDs 2019 monthly emission.

37

38 A summary of S emissions under different scenarios is provided in Table S1. For each set of  
 39 experiments, there are three scenarios: full ship emissions, reduced ship emissions using the

1 IMO2020 standards, and no ship emission of S. Other emissions are kept the same. We take the  
 2 difference in aerosol loading between with full ship emissions of SO<sub>2</sub> and with reduction due to  
 3 IMO2020 as the impact of IMO2020. The difference in aerosol loading is translated into N<sub>d</sub>  
 4 changes with method in the following subsection.

5

### 6 *b) Deep learning-based N<sub>d</sub>*

7 The operational version of NASA’s Global Earth Observing System (GEOS) runs single moment  
 8 cloud and aerosol microphysical schemes. They do not predict cloud condensation nuclei (CCN)  
 9 and cloud droplet number concentrations (N<sub>d</sub>). We estimate N<sub>d</sub> using a diagnostic deep learning-  
 10 based approach, involving the usage of two neural network (NN) parameterizations. The first NN  
 11 (termed MAMnet) is an emulator for the Modal Aerosol Module, which takes bulk aerosol mass  
 12 for 5 externally-mixed species (sulfates, sea salt, dust, black carbon, and organics) and the  
 13 atmospheric state (temperature, pressure) as input, and predicts the number concentration and  
 14 composition for 7 internally-mixed lognormal modes (accumulation, aitken, coarse/fine dust,  
 15 coarse/fine sea salt, primary carbon matter). MAMnet was trained on 5 years of data from a  
 16 GEOS simulation implementing the MAM7 aerosol module, and validated against ground  
 17 observations. The CCN concentration at a given supersaturation can be readily estimated using  
 18 the 7-modal size distribution and composition<sup>45</sup>. A second NN model (Wnet) is used to estimate  
 19 N<sub>d</sub>. Estimation of N<sub>d</sub> requires the characteristic vertical wind velocity (W) at the scale of  
 20 individual parcels, typically proportional to its subgrid-scale standard deviation (σ<sub>w</sub>). Wnet  
 21 takes the atmospheric state, as well as coarse metrics of turbulence (Richardson number and total  
 22 scalar diffusivity) as inputs and predicts σ<sub>w</sub> for each grid cell. Wnet was trained on 2 years of a  
 23 global, non-hydrostatic, storm-resolving simulation of the GEOS model and physically  
 24 constrained by ground-based observations of σ<sub>w</sub> from around the world using a novel generative  
 25 approach<sup>46</sup>. The aerosol size distribution predicted from MAMnet as well as σ<sub>w</sub> are used to  
 26 predict N<sub>d</sub> using the Abdul-Razzak and Ghan scheme<sup>47</sup>. Our NN-based method emphasizes  
 27 observations and conservation of known physics during the development of the NNs and ensures  
 28 a robust prediction of CCN and N<sub>d</sub>.

### 29 *c) Calculating aerosol indirect forcing*

30

31 We use the same methodology reported in Yuan et al. (2023)<sup>21</sup>. We consider the Twomey effect  
 32 and effects of cloud fraction and LWP adjustments. Without considering aerosol effects on cloud  
 33 fractions, cloud albedo sensitivity to aerosols can be taken as the sum of the Twomey effect and  
 34 aerosol induced LWP adjustments:

$$35 \quad S = \frac{dA_c}{dN_d} = \frac{A_c(1-A_c)}{3N_d} \times \left(1 + \frac{5}{2} \frac{d \ln LWP}{d \ln N_d}\right) \quad (1)$$

36 where S is the susceptibility of cloud albedo (A<sub>c</sub>) to droplet number concentration N<sub>d</sub><sup>16</sup>.

37

38 We then have

$$39 \quad \Delta SW_{TOA} = - SW_{downwelling} \times Cf \times S \times \Delta N_d \quad (2)$$

40

41 Aerosol indirect forcing from the Twomey effect and LWP adjustment is therefore:

$$42 \quad \Delta SW_{TOA} = - SW_{downwelling} \times Cf \times A_c \times (1 - A_c) \times \left(\frac{1}{3} + \frac{5}{6} \frac{d \ln LWP}{d \ln N_d}\right) \times \Delta \ln N_d \quad (3).$$

43

1 To consider the effect of Cf adjustment due to aerosols, we consider the sensitivity of scene  
 2 albedo (A) to  $N_d$ .  $A = A_{ac} C_{f_{total}} + A_s(1 - C_{f_{total}})$ . We have:

$$3 \quad S^* = \frac{dA}{dN_d} = \frac{d(A_{ac} C_{f_{total}} + A_s(1 - C_{f_{total}}))}{dN_d} \approx C_f \times S + (1 - C_{f_{high}}) \times \frac{dC_f}{dN_d} \times (A_{ac} - A_s) \quad (4)$$

4 where A is the scene albedo, i.e., including both cloudy,  $A_{ac}$ , and clear,  $A_s$ , parts;  $C_{f_{total}}$  and  $C_f$   
 5 are all cloud and low cloud fraction obtained from the MYD08\_M3 data;  $A_s$  is the surface  
 6 albedo, derived from the CERES EBAF-TOA data<sup>48</sup>;  $1 - C_{f_{high}}$  is used to take into account of  
 7 effect of overlap on Cf adjustment. We assume a maximum overlap between high and low  
 8 clouds. We assume minimum aerosol effects on high clouds. The estimation is done at monthly  
 9 time scales.

10  
 11 CF and LWP adjustments,  $\frac{dC_f}{dN_d}$  and  $\frac{d \ln LWP}{d \ln N_d}$ , are derived from our previous work based on large  
 12 number of ship-track samples<sup>21</sup>. The assumption is that clouds with similar properties respond  
 13 similarly to addition of aerosols and ship-tracks detected under diverse background cloud  
 14 conditions can be used to effectively derive these adjustments. Our results are based on the  
 15 responses from observed ship-track sampled under diverse set of environmental conditions,  
 16 which allows us to derive robust cloud adjustments based on numerous ship-track samples<sup>21</sup>.  
 17 There are a few assumptions and approximations as noted in our previous study<sup>21</sup> and we  
 18 reiterate them here. We used  $SW_{downwelling}$  at the surface from CERES instead of  $SW_{downwelling}$  at  
 19 the cloud top, which underestimates the total forcing since  $SW_{downwelling}$  at the cloud top is larger.  
 20 The LWP and Cf adjustments can be sensitive to more variables that those considered here. We  
 21 assume the derived  $\frac{dC_f}{dN_d}$  and  $\frac{d \ln LWP}{d \ln N_d}$  and their dependence on background variables apply to  
 22 regions that have less ship-track samples. Also, potential semi-direct effects due to absorbing  
 23 aerosols from ship-emissions are not explicitly addressed in this study since we do not have  
 24 enough observations.

25  
 26  
 27 The cloud adjustments used here can depend on the background cloud  $N_d$ , SST, EIS, and  
 28 background  $N_d$  and thus they have spatiotemporal variations due to background changes. The  
 29 dependence of cloud adjustments can also be parameterized with one or more variables. The  $N_d$ -  
 30 only functional form provides a lower bound on the forcing calculation<sup>21</sup> and we explore  
 31 different 2-variable combinations to provide a range of estimates. We combine the cloud  
 32 adjustments with the simulated  $\Delta N_d$  due to IMO2020 and observations of clouds and other  
 33 parameters in 2020 to calculate its forcing. We report the mean forcing from all five functional  
 34 forms of cloud adjustments as well as the standard deviation. We also report the warming effect  
 35 expected from both the upper and lower bounds in Figure 3. Due to the  $N_d$ -dependent nature of  
 36 cloud adjustments, the same  $\Delta N_d$  can result in different magnitude of radiative forcing<sup>21,49</sup>.

37  
 38 There is systematic difference between GEOS-modeled and MODIS observed climatology of  $N_d$ .  
 39 At each grid point, we calculate the ratio between modeled and observed  $N_d$  based on monthly  
 40 data and scale the modeled  $\Delta N_d$  with the ratio before using above equations to calculate the  
 41 forcing. The global mean values change by 10% between scaled and non-scaled  $\Delta N_d$ , all coming  
 42 from the CF adjustment since the LWP adjustment and the Twomey effect depend on  $\Delta N_d/N_d$   
 43 that does not change with scaling. Regionally, the difference can be as large as 30%, e.g., in the  
 44 Southeast Atlantic.

1  
 2 The CERES EBAF-TOA data<sup>48</sup> provides monthly and climatological averages of observed top-  
 3 of-atmosphere and computed cloud radiative effect and absorbed solar radiation. The top-of-  
 4 atmosphere net fluxes provides constraints to the ocean heat storage. It is used here to calculate  
 5 the interhemispheric contrast in absorbed solar radiation and energy balance. We note that  
 6 although the interhemispheric contrast is a residue of two large numbers, e.g., the amount of  
 7 mean absorbed solar radiation in both hemispheres, the observed variation of the contrast is  
 8 always small. Therefore, even though we cannot directly attribute the variations in the  
 9 interhemispheric contrast to IMO 2020, it is reasonable to discuss their temporal evolutions and  
 10 compare the IMO 2020 impact with the observed changes.

11  
 12 *d) Transient warming of IMO2020*

13  
 14 We consider the simple one-layer energy balance model<sup>27</sup>:

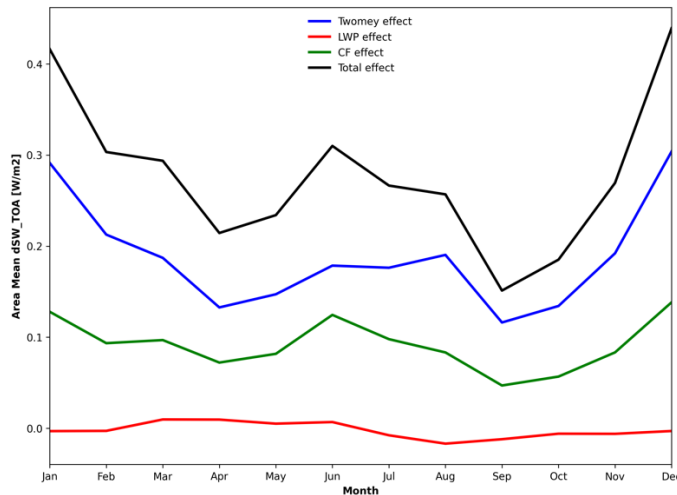
$$15 \quad C \times \frac{dT}{dt} = F - \lambda \times T \quad (5)$$

16 where C is the heat capacity of the well-mixed ocean layer, T is the temperature anomaly from  
 17 the equilibrium, t is time, F is the forcing, and  $\lambda$  is the climate feedback parameter. For an abrupt  
 18 forcing, the solution is:

$$19 \quad T = (F/\lambda) \times (1 - e^{-\lambda t/c}) \quad (6).$$

20 Using  $C = 8.2 \text{ W yr/m}^2/\text{K}$  and  $\lambda = 1.2 \text{ Wm}^{-2}\text{K}^{-1}$ , for a forcing of  $F = 0.2 \text{ Wm}^{-2}$ , we get the  
 21 temperature change at the new equilibrium is 0.17K with a time scale of  $C/\lambda = 7$  years. The  
 22 warming rate is  $F/C = 0.2/8.2 \text{ K/yr} = 0.024 \text{ K/yr}$  or 0.24 K/decade.  $\lambda$  has uncertainty associated  
 23 with it and its  $1-\sigma$  is  $0.25 \text{ Wm}^{-2}\text{K}^{-1}$ . With this, we can estimate equilibrium T to be between 0.14  
 24 and 0.21 K. Equation 6 is used to calculate the expected warming trajectory in the 2020s when  
 25 combined with a simple long-term upward trend in Figure 3. The observed global mean  
 26 temperature is from the National Aeronautics and Space Administration (NASA) Goddard  
 27 Institute of Space Studies.

28  
 29 *e) Contributions of background  $N_d$ , CF, and  $\Delta N_d$*



1 **Figure S1: Seasonal variations of areal mean radiative forcing over the North Atlantic if a**  
2 **seasonally invariant incoming solar isolation (annual mean at each grid) is used. The peak**  
3 **in the summertime in Figure 3 is replaced by a wintertime peak.**

4  
5 We calculate the annual mean of incoming solar radiation for each oceanic grid in the North  
6 Atlantic and use this map of seasonally invariant incoming solar radiance to calculate IMO2020  
7 forcing (see section c of Methods). The seasonal cycle of forcing using the seasonally invariant  
8 solar radiation is shown in Figure S1, which differs substantially from Figure 3a, highlighting the  
9 impact of seasonal cycle in solar radiation. The peak season for the forcing is now wintertime  
10 instead of summertime. This serves as our baseline to test sensitivity of forcing to different  
11 variables.

12  
13 The sensitivity of the forcing to each factor is assessed through the following procedure. We first  
14 calculate the seasonal variations of the forcing using observations that contain its seasonal  
15 variations. We then calculate a map of annual mean for each variable and use it to calculate the  
16 forcing, effectively removing its impact on the seasonal changes. The relative difference between  
17 these two calculations can be taken as a measure of how much each variable contributes to the  
18 seasonal changes.

19  
20 **Data Availability Statement:**

21 MODIS, CERES, and MERRA-2 data are public available at their respective websites:  
22 <https://ladsweb.modaps.eosdis.nasa.gov/> , <https://ceres.larc.nasa.gov/> ,  
23 [https://gmao.gsfc.nasa.gov/reanalysis/MERRA-2/data\\_access/](https://gmao.gsfc.nasa.gov/reanalysis/MERRA-2/data_access/). The GOCART simulation data  
24 can be found here:  
25 <https://dataverse.harvard.edu/dataset.xhtml?persistentId=doi:10.7910/DVN/H0ZFK9>.

26  
27 **Code Availability Statement:**

28 The codes are available here: <https://zenodo.org/records/11094677>.

29  
30 **Competing Interests Statement:**

31 The authors declare no competing interests.

32  
33 **Author Contributions:**

34 T. Y. conceived the idea, designed the experiments, and wrote the draft. H.S. analyzed the data  
35 and made plots. H.B. and K.B. ran simulations. All authors contributed to writing and revising  
36 the manuscript.

37  
38 **Reference:**

- 39 1. Forster, P. *et al.* The Earth's Energy Budget, Climate Feedbacks, and Climate Sensitivity. in  
40 *Climate Change 2021: The Physical Science Basis. Contribution of Working Group I to the*  
41 *Sixth Assessment Report of the Intergovernmental Panel on Climate Change* (Cambridge  
42 University Press, 2021).

- 1 2. Bellouin, N. *et al.* Bounding Global Aerosol Radiative Forcing of Climate Change. *Reviews*  
2 *of Geophysics* **58**, e2019RG000660 (2020).
- 3 3. Crutzen, P. J. Albedo Enhancement by Stratospheric Sulfur Injections: A Contribution to  
4 Resolve a Policy Dilemma? *Climatic Change* **77**, 211–220 (2006).
- 5 4. National Academies of Sciences, E., and Medicine. *Reflecting Sunlight: Recommendations*  
6 *for Solar Geoengineering Research and Research Governance*. (The National Academies  
7 Press, Washington, DC, 2021). doi:10.17226/25762.
- 8 5. Robock, A., Marquardt, A., Kravitz, B. & Stenchikov, G. Benefits, risks, and costs of  
9 stratospheric geoengineering. *Geophysical Research Letters* **36**, (2009).
- 10 6. Jones, A., Haywood, J. & Boucher, O. Climate impacts of geoengineering marine  
11 stratocumulus clouds. *Journal Of Geophysical Research-Atmospheres* **114**, D10106 (2009).
- 12 7. Bala, G. *et al.* Albedo enhancement of marine clouds to counteract global warming: impacts  
13 on the hydrological cycle. *Clim Dyn* **37**, 915–931 (2011).
- 14 8. Latham, J. *et al.* Marine cloud brightening. *Philosophical Transactions of the Royal Society*  
15 *A: Mathematical, Physical and Engineering Sciences* **370**, 4217–4262 (2012).
- 16 9. Wood, R. Assessing the potential efficacy of marine cloud brightening for cooling Earth  
17 using a simple heuristic model. *Atmospheric Chemistry and Physics Discussions* 1–52 (2021)  
18 doi:10.5194/acp-2021-327.
- 19 10. Conover, J. H. Anomalous cloud lines. *Journal Of The Atmospheric Sciences* **23**, 778–785  
20 (1966).
- 21 11. Coakley, J. A., Bernstein, R. L. & Durkee, P. A. Effect of Ship-Stack Effluents on Cloud  
22 Reflectivity. *Science* **237**, 1020–1022 (1987).

- 1 12. Twomey, S. Influence of pollution on shortwave albedo of clouds. *Journal Of The*  
2 *Atmospheric Sciences* **34**, 1149–1152 (1977).
- 3 13. Albrecht, B. Aerosols, Cloud Microphysics, and Fractional Cloudiness. *Science* **245**, 1227  
4 (1989).
- 5 14. Wang, H., Rasch, P. J. & Feingold, G. Manipulating marine stratocumulus cloud amount and  
6 albedo: a process-modelling study of aerosol-cloud-precipitation interactions in response to  
7 injection of cloud condensation nuclei. *Atmospheric Chemistry And Physics* **11**, 4237–4249  
8 (2011).
- 9 15. Christensen, M. W. & Stephens, G. L. Microphysical and macrophysical responses of marine  
10 stratocumulus polluted by underlying ships: Evidence of cloud deepening. *Journal of*  
11 *Geophysical Research* **116**, D03201 (2011).
- 12 16. Toll, V., Christensen, M., Quaas, J. & Bellouin, N. Weak average liquid-cloud-water response  
13 to anthropogenic aerosols. *Nature* **572**, 51–55 (2019).
- 14 17. International Maritime Organization. IMO 2020 Sulfur Oxide Emission Regulation. (2020).
- 15 18. Yuan, T. *et al.* Global reduction in ship-tracks from sulfur regulations for shipping fuel.  
16 *Science Advances* **8**, eabn7988 (2022).
- 17 19. Diamond, M. S. Detection of large-scale cloud microphysical changes within a major  
18 shipping corridor after implementation of the International Maritime Organization 2020 fuel  
19 sulfur regulations. *Atmospheric Chemistry and Physics* **23**, 8259–8269 (2023).
- 20 20. Diamond, M. S., Director, H. M., Eastman, R., Possner, A. & Wood, R. Substantial Cloud  
21 Brightening From Shipping in Subtropical Low Clouds. *AGU Advances* **1**, e2019AV000111  
22 (2020).

- 1 21. Yuan, T. *et al.* Observational Evidence of Strong Forcing from Aerosol Effect on Low Cloud  
2 Coverage. *Science Advances* **9**, (2023).
- 3 22. Capaldo, K., Corbett, J. J., Kasibhatla, P., Fischbeck, P. & Pandis, S. N. Effects of ship  
4 emissions on sulphur cycling and radiative climate forcing over the ocean. *Nature* **400**, 743–  
5 746 (1999).
- 6 23. Lauer, A., Eyring, V., Hendricks, J., Jöckel, P. & Lohmann, U. Global model simulations of  
7 the impact of ocean-going ships on aerosols, clouds, and the radiation budget. *Atmospheric*  
8 *Chemistry and Physics* **7**, 5061–5079 (2007).
- 9 24. Peters, K., Stier, P., Quaas, J. & Graßl, H. Aerosol indirect effects from shipping emissions:  
10 sensitivity studies with the global aerosol-climate model ECHAM-HAM. *Atmospheric*  
11 *Chemistry and Physics* **12**, 5985–6007 (2012).
- 12 25. Partanen, A. I. *et al.* Climate and air quality trade-offs in altering ship fuel sulfur content.  
13 *Atmospheric Chemistry and Physics* **13**, 12059–12071 (2013).
- 14 26. Gettelman, A. *et al.* Reducing Ship Emissions Accelerates Global Warming. in *AEROCOM-*  
15 *AEROSAT 2023* (Richland, WA, 2023).
- 16 27. Geoffroy, O. *et al.* Transient Climate Response in a Two-Layer Energy-Balance Model. Part  
17 I: Analytical Solution and Parameter Calibration Using CMIP5 AOGCM Experiments.  
18 *Journal of Climate* **26**, 1841–1857 (2013).
- 19 28. Record-breaking North Atlantic Ocean temperatures contribute to extreme marine heatwaves  
20 | Copernicus. [https://climate.copernicus.eu/record-breaking-north-atlantic-ocean-](https://climate.copernicus.eu/record-breaking-north-atlantic-ocean-temperatures-contribute-extreme-marine-heatwaves)  
21 [temperatures-contribute-extreme-marine-heatwaves.](https://climate.copernicus.eu/record-breaking-north-atlantic-ocean-temperatures-contribute-extreme-marine-heatwaves)
- 22 29. Loeb, N. G. *et al.* Satellite and Ocean Data Reveal Marked Increase in Earth’s Heating Rate.  
23 *Geophysical Research Letters* **48**, e2021GL093047 (2021).

- 1 30. IPCC. Summary for Policymakers, in: Global Warming of 1.5 C. (2018).
- 2 31. Lee, T. & Romero, J. IPCC, 2023: Summary for Policymakers. in *Climate Change 2023:*  
3 *Synthesis Report. Contribution of Working Groups I, II and III to the Sixth Assessment Report*  
4 *of the Intergovernmental Panel on Climate Change* 1–34 (IPCC, Geneva, Switzerland,  
5 2023).
- 6 32. Turnock, S. T. *et al.* The Future Climate and Air Quality Response From Different Near-  
7 Term Climate Forcer, Climate, and Land-Use Scenarios Using UKESM1. *Earth's Future* **10**,  
8 e2022EF002687 (2022).
- 9 33. Possner, A., Wang, H., Wood, R., Caldeira, K. & Ackerman, T. P. The efficacy of aerosol-  
10 cloud radiative perturbations from near-surface emissions in deep open-cell stratocumuli.  
11 *Atmospheric Chemistry and Physics* **18**, 17475–17488 (2018).
- 12 34. Christensen, M. W. *et al.* Opportunistic experiments to constrain aerosol effective radiative  
13 forcing. *Atmospheric Chemistry and Physics* **22**, 641–674 (2022).
- 14 35. Manshausen, P., Watson-Parris, D., Christensen, M. W., Jalkanen, J.-P. & Stier, P. Invisible  
15 ship tracks show large cloud sensitivity to aerosol. *Nature* **610**, 101–106 (2022).
- 16 36. Glassmeier, F. *et al.* Aerosol-cloud-climate cooling overestimated by ship-track data. *Science*  
17 **371**, 485–489 (2021).
- 18 37. Ceppi, P., Brient, F., Zelinka, M. D. & Hartmann, D. L. Cloud feedback mechanisms and  
19 their representation in global climate models. *Wiley Interdisciplinary Reviews-Climate*  
20 *Change* **8**, (2017).
- 21 38. Yuan, T., Oreopoulos, L., Platnick, S. E. & Meyer, K. Observations of Local Positive Low  
22 Cloud Feedback Patterns and Their Role in Internal Variability and Climate Sensitivity.  
23 *Geophysical Research Letters* **45**, 4438–4445 (2018).

- 1 39. Chin, M. *et al.* Multi-decadal aerosol variations from 1980 to 2009: a perspective from  
2 observations and a global model. *Atmospheric Chemistry and Physics* **14**, 3657–3690 (2014).
- 3 40. Bian, H. *et al.* Observationally constrained analysis of sea salt aerosol in the marine  
4 atmosphere. *Atmospheric Chemistry and Physics* **19**, 10773–10785 (2019).
- 5 41. Gelaro, R. *et al.* The Modern-Era Retrospective Analysis for Research and Applications,  
6 Version 2 (MERRA-2). *J. Climate* **30**, 5419–5454 (2017).
- 7 42. Hoesly, R. M. *et al.* Historical (1750–2014) anthropogenic emissions of reactive gases and  
8 aerosols from the Community Emissions Data System (CEDS). *Geoscientific Model*  
9 *Development* **11**, 369–408 (2018).
- 10 43. Darmenov, A. & da Silva, A. The Quick Fire Emissions Dataset (QFED) - Documentation of  
11 versions 2.1, 2.2 and 2.4. *NASA TM-2015-104606* **38**, 183 (2015).
- 12 44. Forster, P. M. *et al.* Current and future global climate impacts resulting from COVID-19.  
13 *Nat. Clim. Chang.* **10**, 913–919 (2020).
- 14 45. Fountoukis, C. & Nenes, A. Continued development of a cloud droplet formation  
15 parameterization for global climate models. *Journal Of Geophysical Research-Atmospheres*  
16 **110**, D11212 (2005).
- 17 46. Barahona, D., Breen, K., Kalesse-Los, H. & Rottenbacher, J. Deep learning parameterization  
18 of small-scale vertical velocity variability for atmospheric models. *Artificial Intelligence for*  
19 *the Earth Systems* (2023).
- 20 47. Abdul-Razzak, H. & Ghan, S. J. A parameterization of aerosol activation: 2. Multiple aerosol  
21 types. *Journal of Geophysical Research: Atmospheres* **105**, 6837–6844 (2000).

- 1 48. Loeb, N. G. *et al.* Clouds and the Earth’s Radiant Energy System (CERES) Energy Balanced  
2 and Filled (EBAF) Top-of-Atmosphere (TOA) Edition-4.0 Data Product. *Journal of Climate*  
3 **31**, 895–918 (2018).
- 4 49. Gryspeerdt, E. *et al.* Uncertainty in aerosol–cloud radiative forcing is driven by clean  
5 conditions. *Atmospheric Chemistry and Physics* **23**, 4115–4122 (2023).

6  
7  
8 **Figure 1 Simulated impact of IMO2020 on AOD and  $N_d$ . a) simulated annual mean aerosol**  
9 **optical depth change induced by IMO2020 using NASA GOES-GOCART. b) the ratio of**  
10 **aerosol optical depth changes between that induced by IMO2020 and that between 1750**  
11 **and 2005<sup>2</sup>. c) map of simulated annual mean  $N_d$  change due to IMO2020. d) same as b, but**  
12 **for  $N_d$  change.**

13  
14 **Figure 2: Calculated IMO2020 forcing maps from different components. The spatial**  
15 **patterns of three components of forcing from cloud adjustments: a) the Twomey effect, b)**  
16 **LWP adjustment, and c) cloud fraction adjustment.**

17  
18 **Figure 3: Time series of global temperature anomaly since the 1980 (Lensen et al., 2019).**  
19 **The trend line is dashed. The expected warming trajectory from the combination of the**  
20 **linear trend and the calculated warming effect from IMO 2020 shock based on the energy**  
21 **balance model. The upper and lower bounds of the expected warming are shown in shades.**  
22 **The baseline period for temperature anomaly is between 1951 and 1980.**

23  
24 **Figure 4: Sensitivity of forcing components to different cloud variables. a) The areal mean**  
25 **of forcing from IMO2020 in the North Atlantic (0°-80°W, 0° ~ 60°N) and its break down in**  
26 **three components. b-d) sensitivity tests to gauge the impacts of seasonal variations in  $\Delta N_d$ ,**  
27 **background  $N_d$ , and cloud fraction, respectively. In each test, we use an annual mean map**  
28 **instead of seasonally changing fields to calculate the radiative forcing and plot their**  
29 **difference from the baseline. Details in Methods section.**

30  
31 **Figure 5: Observed time series of energy balance variables. A) the planetary heat uptake;**  
32 **B) trailing 48-month mean of absorbed solar radiation for both hemispheres. The 48-month**  
33 **mean is applied to remove high-frequency noise. C) Time series of Interhemispheric**  
34 **contrast in absorbed solar radiation. The vertical dotted line marks the Jan 2020. Details in**  
35 **Methods section.**

36